RESEARCH ARTICLE | MAY 10 2022

Effect of contact angles on dynamical characteristics of the annular focused jet between parallel plates

Jian Huang (黄荐); Guanghang Wang (王广航); Yiwei Wang (王一伟); ... et. al

Physics of Fluids 34, 052107 (2022)
https://doi.org/10.1063/5.0090696

Physics of Fluids ARTICLE scitation.org/journal/phf

Effect of contact angles on dynamical characteristics of the annular focused jet between parallel plates

Cite as: Phys. Fluids **34**, 052107 (2022); doi: 10.1063/5.0090696
Submitted: 8 March 2022 · Accepted: 20 April 2022 ·
Published Online: 10 May 2022

View Online Export Citation CrossMark

Jian Huang (黄荐),[1] Guanghang Wang (王广航),[1,2] Yiwei Wang (王一伟),[1,2] Jingzhu Wang (王静竹),[1,2,a)] and Zhaohui Yao (姚朝晖)[1,a)]

AFFILIATIONS

[1]School of Engineering Science, University of Chinese Academy of Science, Beijing 101408, People's Republic of China
[2]Key Laboratory for Mechanics in Fluid Solid Coupling Systems, Institute of Mechanics, Chinese Academy of Sciences, Beijing 100190, People's Republic of China

[a)]**Authors to whom correspondence should be addressed:** wangjingzhu@imech.ac.cn and yaozh@ucas.edu.cn

ABSTRACT

Focused jets have been widely studied owing to the abundance of attractive flow phenomena and industrial applications, whereas annular focused jets are less studied. This study combines experiments, numerical simulations, and analytical modeling to investigate the effect of the contact angle on the generation position and focusing efficiency of annular focused jets between parallel plates. In the experiment, a pulsed laser generates a cavitation bubble inside the droplet, and the rapidly expanding cavitation bubble drives an annular-focused jet on the droplet surface. Changing the plate wettability creates different contact angles and droplet surface shapes between the droplet and plates, which modulates the position and focusing efficiency of the annular jet. Based on the jet singularity theory and by neglecting gravity, the derived formula for the jet position offset is found to depend only on the contact angle, which is in good agreement with the experimental and numerical simulation results. Combined with numerical simulations to analyze the flow characteristics of the droplets between the parallel plates, a new calculation method for the jet focusing efficiency is proposed. Interestingly, when the liquid surface radius is small, the focusing efficiency can be improved by adjusting the contact angle to make the jet position closer to the flat plate, whereas the same operation reduces the focusing efficiency when the radius is large. The study of annular jets can expand the scope of traditional jet research and has the potential to provide new approaches for applications such as high-throughput inkjet printing and liquid transfer.

I. INTRODUCTION

Focused jets are a widespread flow phenomenon that can occur in instances encompassing microscopic-scale fluids to the macroscopic structures of the universe.[1] Typical jets include droplets dripping into the liquid pool,[2–4] bubbles bursting,[5,6] bubbles shedding,[7] fluctuations on the liquid surface,[8] and impact effects on the liquid surface.[9–11] Focused jets are also widely used in many industrial fields, such as micro-jet research, which is the key to developing needle-free injections[12–14] and inkjet printing.[15–17] Liquid transfer using micro-jet technology ensures that the viability of the biological samples is not affected,[18] and the smallest transferred droplets can reach the nanometer level.[19] Additionally, these findings could serve for drug screening and cellular tissue culture. The micro-jets enable smaller diameters and faster speeds by adjusting the initial shape of the fluid surface.[20] For inkjet printing, finer micro-jets result in higher printing accuracy.[21] For needle-free injections, finer and faster micro-jets have better skin penetration properties, which can reduce the skin trauma area[22,23] and obtain higher drug dispersion in the subcutaneous tissue.[24] Studies have also demonstrated that liquid surfaces with initial shapes, such as Faraday waves,[25] can reduce the energy required for the liquid transfer.

The aforementioned focused jets have the same generation mechanism, namely, flow focusing. A concave surface causes the fluid to form a convergent flow. Convergent fluids squeeze each other, converting radial kinetic energy into axial kinetic energy, resulting in a local high-speed flow, that is, a focused jet.[26,27] Antkowiak *et al.* found that no jet occurred when water and sand had no initial concave surface in a test tube drop test. Conversely, it occurred when the liquid surface had a meniscus or bubble or when the sand surface had a hemispherical crater.[6] Another experiment had similar results, in

which a hollow sphere half filled with water fell freely, hit the ground, and bounced off. During the ascent after the first rebound, the liquid surface became concave and sustained until the second rebound; therefore, a jet was formed on the liquid surface after the second rebound.[28] Moreover, the shape of the liquid surface controls the direction and velocity of the jet.[29,30] Therefore, the shape of the liquid surface is an essential breakthrough point for studying the formation mechanisms and evolutionary processes of a focused jet.

In existing studies, the focused jets are predominantly cylindrical, and the corresponding liquid surface shapes are curved surfaces with positive Gaussian curvatures such as menisci and spherical surfaces. When the surface shape is not center-symmetric, the jet shape is no longer a standard cylindrical shape such as generating a flat sheet jet in a rectangular liquid tank.[31] The focused jet formed by the surface with zero Gaussian curvature is sheet-shaped, and the focused jet generated by the surface with negative Gaussian curvature is annular. The coronal secondary jet produced by the collapse of cavitation bubbles near the free surface is a typical annular jet.[32,33] Annular jets are superior to column jets in terms of jet flux and have exhibited excellent potential for inkjet printing and drug preparation;[34] however, annular jets have not been systematically studied.

In this study, droplets were injected between parallel plates with a small gap, and the droplets contacted both plates and eventually formed stable contact angles. By changing the wettability of the plates, variable contact angles can be obtained, resulting in different shapes of the droplet sides, including cylindrical surfaces and negative Gaussian surfaces (saddle surfaces).[35,36] A pulsed laser was focused on the center of the droplet, and the resulting bubble induced the droplet to form an annular focused jet. First, we obtained the relationship between the curvature radius of the liquid surface and the contact angles without gravity. Subsequently, the generation position of the jet was deduced, and a prediction model for the jet focusing efficiency was established. On this basis, the central point of discussion is the influence of the contact angles on the generation position and focusing efficiency of the annular jets between the plates.

II. RESEARCH METHODOLOGY

A. Experimental setup

Figure 1(a) shows the schematic of the experimental setup. The material of the plate is transparent acrylic with a thickness of 5 mm, and the gap (H) between the two plates is 0.8 mm. Deionized water was slowly injected between the two plates using a syringe to form a columnar droplet with a diameter of approximately 12 mm in contact with both the upper and lower plates. To obtain different contact angles, three types of surface preparations were prepared: no coating, hydrophobic coating (N319, Nanocoating, Jiangsu, China), and superhydrophilic coating (NC3082, Nanocoating, Jiangsu, China). The combination of the three types of upper and lower plates allows the droplets to have varying contact angles.

To better absorb the laser energy, an aluminum foil with a side length and width of 1.8 mm and a thickness of 0.1 mm was pasted on the plate below the center of the droplet, as shown in Fig. 1(b). The pulsed laser was generated by an Nd:YAG laser (Quanta-Ray Pro, Spectra-Physics, CA, USA) with a wavelength of 1064 nm, a single pulse duration of 10 ns, and a laser energy of approximately 0.9 J. The horizontal laser beam was first converted to a vertically upward direction by a mirror inclined at a 45° angle and then focused on the aluminum foil by a horizontally placed hemispherical lens. The diameter of the laser spot focused on the aluminum foil was approximately 0.5 mm. Experiments demonstrated that the experimental results of the aluminum foil attached to the inner side of the lower plate were the same as those attached to the upper plate.

The annular jet morphology was precisely recorded using a high-speed camera (Phantom V1612, Vision Research Ltd., USA) equipped with a microscope lens with an image resolution of approximately 14.8 μm/pixel. For a detailed recording of the complete jet evolution, the camera sampling frequency was set up to 200 000 fps, and a computer-controlled delayed capture technique was employed. Figures 1(b) and 1(c) show the top and side views, respectively, of the annular jet captured in the experiment. To simultaneously acquire the jet velocity and position, shots were mainly taken from the side, as shown in Fig. 1(a), with high-brightness light-emitting diodes and cameras on each side of the droplet.

B. Numerical simulation

Numerical calculations were performed to simulate the evolution processes of the annular focused jet between parallel plates using OpenFOAM. The volume of fluid (VOF) and large-eddy simulation (LES) methods were applied to capture the gas–liquid interface and

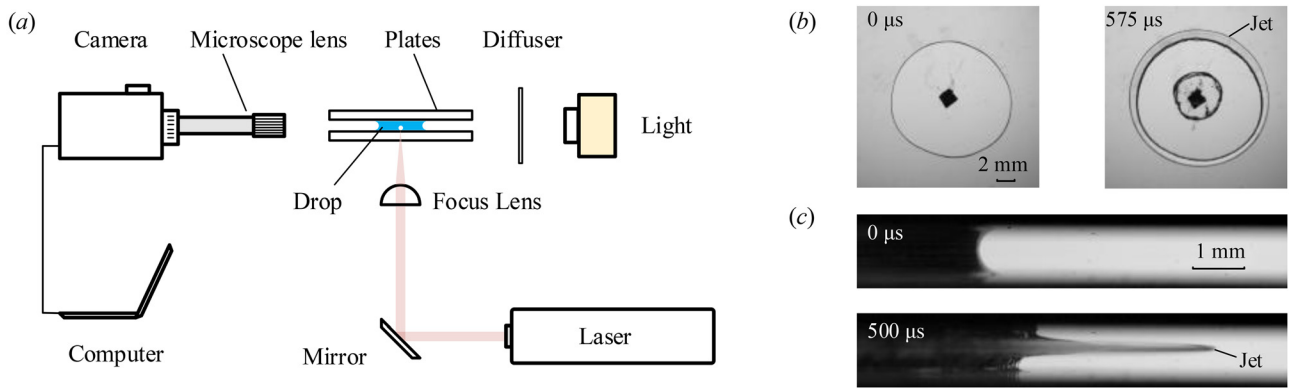

FIG. 1. Experimental setup and typical results for the annular jets between parallel plates. (a) Optical setup used to generate and observe the annular jets. (b) Top view of the annular jet. (c) Side view of the annular jet.

the fine flow structure.[37,38] In the simulation, the gas and liquid phases were defined as compressible Newtonian fluids,[39] considering the heat transfer. The equations for continuity, momentum, and energy are as follows:

$$\frac{\partial \rho}{\partial t} + \nabla \cdot (\rho \boldsymbol{U}) = 0, \tag{1}$$

$$\frac{\partial}{\partial t}(\rho \boldsymbol{U}) + \nabla \cdot (\rho \boldsymbol{U}\boldsymbol{U}) = -\nabla\left(p + \frac{2\mu}{3}\nabla \cdot \boldsymbol{U}\right) + \nabla \cdot \left[\mu\left(\nabla \boldsymbol{U} + (\nabla \boldsymbol{U})^{\mathrm{T}}\right)\right] + \gamma\kappa\nabla\alpha, \tag{2}$$

$$\frac{\partial}{\partial t}(\rho C_v T) + \nabla \cdot (\rho C_v T \boldsymbol{U}) - \nabla(\lambda_m C_v \nabla T) = -\nabla \cdot (p\boldsymbol{U}) - \frac{\partial}{\partial t}(\rho k) - \nabla \cdot (\rho k \boldsymbol{U}), \tag{3}$$

where ρ is the mixed density of the fluid; $\rho = \rho_{\mathrm{liquid}}\alpha + \rho_{\mathrm{gas}}(1-\alpha)$, α is the volume fraction of the liquid phase, ∇ is the gradient operator, t is the time, and $\boldsymbol{U}$ is the velocity vector. p is the pressure, and μ is the mixture dynamic viscosity coefficient; $\mu = \mu_{\mathrm{liquid}}\alpha + \mu_{\mathrm{gas}}(1-\alpha)$, μ_{liquid} and μ_{gas} are the dynamic viscosities of the liquid and gas phases, respectively, γ is the surface tension for the gas–liquid interface, and κ is the curvature of the interface. T is the temperature, and C_v is the mixture specific heat capacity; $C_v = C_{v.liquid}\alpha + C_{v.gas}(1-\alpha)$, $C_{v.liquid}$ and $C_{v.gas}$ are the specific heat capacities of the liquid and gas phases, respectively, and λ_m is the heat transfer coefficient for the mixture; $\lambda_m = \lambda_{liquid}\alpha + \lambda_{gas}(1-\alpha)$, λ_{liquid} and λ_{gas} are the heat transfer coefficients for the liquid and gas phases, respectively, and k is the kinetic energy per unit mass, $k = |U|^2/2$.

Assuming that the two phases are homogeneous, the pressure-based implicit splitting of the operators is embedded in the multiphase solver compressibleInterFoam to solve the transient flow problem.[40,41] The transport equation for α is as follows:

$$\frac{\partial \alpha}{\partial t} + \nabla \cdot (\alpha \boldsymbol{U}) + \nabla \cdot (\alpha(1-\alpha)\boldsymbol{U}_r) = 0, \tag{4}$$

where $\boldsymbol{U}_r$ is the relative velocity; $\boldsymbol{U}_r = \boldsymbol{U}_{liquid} - \boldsymbol{U}_{gas}$.

Favre filtering was used to accurately predict large-scale turbulent eddies. Thus, the transport equations for continuity, momentum, energy, and liquid volume fraction are filtered as[42]

$$\frac{\partial \bar{\rho}}{\partial t} + \nabla \cdot (\bar{\rho}\tilde{\boldsymbol{U}}) = 0, \tag{5}$$

$$\frac{\partial}{\partial t}(\bar{\rho}\tilde{\boldsymbol{U}}) + \nabla \cdot (\bar{\rho}\tilde{\boldsymbol{U}}\tilde{\boldsymbol{U}}) = -\nabla\bar{p} + \nabla \cdot \tilde{\boldsymbol{\tau}} + \gamma\kappa\nabla\bar{\alpha} + \nabla \cdot (\bar{\boldsymbol{\tau}} - \tilde{\boldsymbol{\tau}}) + \nabla \cdot \boldsymbol{\tau}_{SGS}, \tag{6}$$

$$\frac{\partial}{\partial t}(\bar{\rho}C_v\tilde{T}) + \nabla \cdot (\bar{\rho}C_v\tilde{T}\tilde{\boldsymbol{U}}) + \frac{\partial}{\partial t}\left(\bar{\rho}\frac{\tilde{\boldsymbol{U}} \cdot \tilde{\boldsymbol{U}}}{2}\right) + \nabla \cdot \left(\bar{\rho}\frac{\tilde{\boldsymbol{U}} \cdot \tilde{\boldsymbol{U}}}{2}\tilde{\boldsymbol{U}}\right) - \nabla(\lambda C_v \nabla T) = \nabla \cdot (\lambda C_v \nabla \tilde{T}) - \nabla \cdot (\bar{p}\tilde{\boldsymbol{U}}) + \nabla \cdot \boldsymbol{H}_{SGS}, \tag{7}$$

$$\frac{\partial \bar{\alpha}}{\partial t} + \nabla \cdot (\bar{\alpha}\tilde{\boldsymbol{U}}) + \nabla \cdot (\bar{\alpha}(1-\bar{\alpha})\tilde{\boldsymbol{U}}_r) = \nabla \cdot \boldsymbol{\beta}_{SGS}, \tag{8}$$

where the superscript "∼" denotes the Favre (density-weighted) filtering, the superscript "−" represents the LES physical space (un-weighted) filtering, the subscript SGS indicates the sub-grid scale, $\boldsymbol{\tau}_{SGS}$ is the stress tensor, $\boldsymbol{H}_{SGS}$ is the heat flux, and $\boldsymbol{\beta}_{SGS}$ is the mass flux. The specific calculation of the above three quantities is referenced to in the study conducted by Ye *et al.*[42] A one-equation eddy-viscosity model was adopted for sub-grid scale modeling, and all partial differential equations were solved using the finite volume method.

The temporal derivatives were discretized using the implicit Euler scheme. The convective terms in the volume fraction equation and the momentum equation were discretized using a second-order van Leer scheme and a second-order upwind scheme, respectively. The other coefficients in the simulations are as follows: the water density $\rho_{0.\mathrm{liquid}}$ is 998 kg m^{-3}; the water dynamic viscosity μ is 1.307 × 10^{-3} Pa s; the surface tension γ is 0.0728 N m^{-1}; specific heat capacities C_v are 4199 J (kg K)$^{-1}$ and 723 J (kg K)$^{-1}$ for water and gas, respectively; the heat conductivities λ_m are 0.599 W (m K)$^{-1}$ and 0.034 W (m K)$^{-1}$ for water and gas, respectively.[43]

As shown in Fig. 2(a), a quarter of the calculation area was selected to improve the calculation efficiency, and its dimensions were 15 × 15 × 0.8 mm^3. The initial bubble was located at the center of the droplet with an initial radius of 0.35 mm and a high intra-bubble pressure (p_0).[44,45] As shown in Figs. 2(b) and 2(c), using the O-block structured grid, the total number of cells was set to approximately 916 800. The grid sizes were initially set to approximately 0.01 and 0.03 mm in the radial direction near the bubble and droplet, respectively. The grids were denser near the solid walls, bubble boundaries, and droplet surfaces to accurately trace the gas–water interface. In the x and y directions, there were approximately 220 cells in each direction. In the z-direction, there were 21 layers of the grid with a cell height of 0.02 mm near the walls. The boundary conditions were set as follows: (i) the two outlet conditions were of constant pressure (1.01 × 10^5 Pa), (ii) the other two sides were symmetrical boundaries, and (iii) the upper and lower walls were no-slip wall boundaries.[43]

C. Theoretical model

The droplet between the two plates is primarily axisymmetric and can be simplified as a two-dimensional axisymmetric model for the purpose of analysis, as shown in Fig. 3.

Because the gap between the plates is small and the effect of gravity is ignored, the two-dimensional Young–Laplace equation for the gas–liquid interface[46] is

$$\left[1 + \left(\frac{dx}{dz}\right)^2\right]^{-3/2}\frac{d^2x}{dz^2} = -\frac{\Delta p}{\gamma}, \tag{9}$$

where Δp is the pressure difference on both sides of the air–liquid interface, which is related to the interface curvature and surface tension coefficient. The side curvature radius of the droplet is much smaller than the annulus radius (6 mm), and the curve of the droplet side is very short. Thus, it can be approximated as an arc,[47] and Eq. (9) can be rewritten as

$$\left[1 + \left(\frac{dx}{dz}\right)^2\right]^{-3/2}\frac{d^2x}{dz^2} = \frac{1}{R}, \tag{10}$$

where R is the side curvature radius of the droplet. In Fig. 3, it is easy to obtain R from the following geometric relationship:

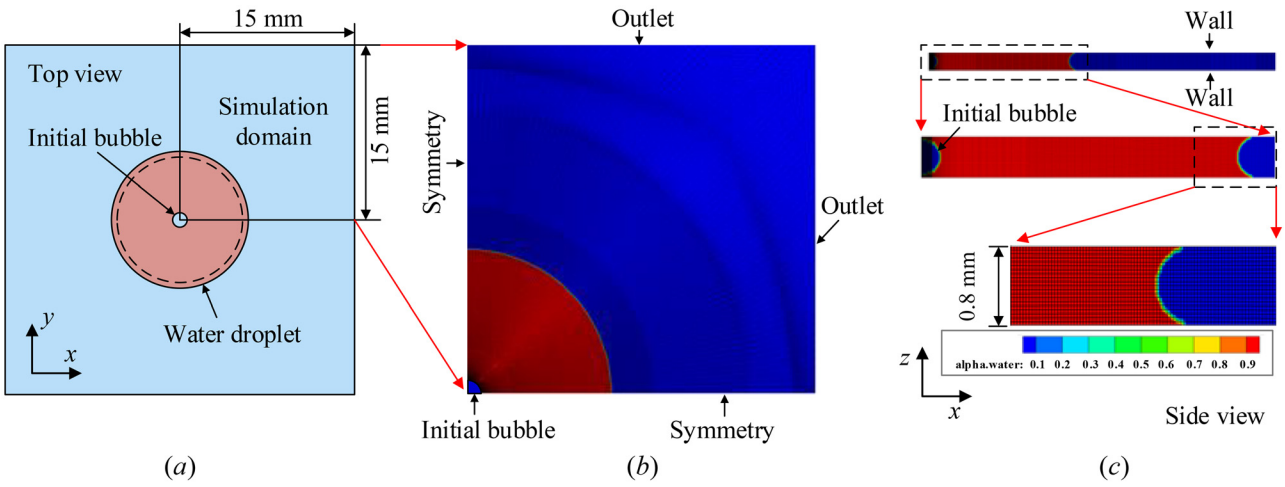

FIG. 2. Mesh setup for numerical simulation. (a) Computational domain. (b) Top view of mesh generation. (c) Side view of mesh generation.

$$R = \frac{H}{\cos\alpha + \cos\beta}, \tag{11}$$

where H is the spacing between the plates and α and β are the liquid contact angles at the lower and upper plates, respectively. This equation can be verified by the study conducted by Teixeira and Teixeira.[48]

The relationship between the derivative of the curve and the inclination angle is

$$\frac{dx}{dz} = -\cot\theta, \tag{12}$$

where θ is the inclination angle of a point at the air–liquid interface. The derivative of Eq. (12) is

$$\frac{d^2x}{dz^2} = \frac{1}{\sin^2\theta}\frac{d\theta}{dz}. \tag{13}$$

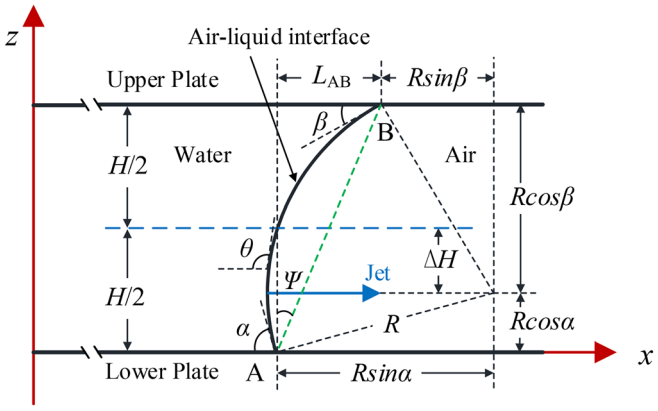

FIG. 3. Sketch of a droplet between the parallel plates: z is the height above the lower plate, x is the radial direction of the droplet, and the origin is located at the center of the droplet on the lower plate. H is the spacing between the upper plate ($z = H$) and the lower plate ($z = 0$), θ is the liquid surface inclination, and α and β are the liquid contact angles at the lower plate and upper plate, respectively ($0 \le \alpha, \beta \le \pi/2$). The blue dashed line indicates the central line of the upper and lower plates, and the distance from each plate is H/2.

Substituting Eqs. (12) and (13) into Eq. (10) yields the following equation:

$$\sin\theta\frac{d\theta}{dz} = \frac{\cos\alpha + \cos\beta}{H}. \tag{14}$$

Integrating Eq. (14) and using $z = 0$, $\theta = \alpha$, Eq. (15) can be obtained as follows:

$$\cos\theta(z) = \cos\alpha - \frac{1}{H}(\cos\alpha + \cos\beta)z. \tag{15}$$

In Fig. 5, the point at which the liquid surface moves first is the extreme point of the liquid surface concavity, namely, the singularity.[49] Here, $\cos\theta = 0$, and in Eq. (15), the location of the jet can be determined as

$$z_{\theta=90^\circ} = \frac{\cos\alpha}{\cos\alpha + \cos\beta}H. \tag{16}$$

Let ΔH be the distance of the jet deviation from the central line, as shown in Fig. 5

$$\Delta H = \frac{|\cos\alpha - \cos\beta|}{2(\cos\alpha + \cos\beta)}H. \tag{17}$$

Furthermore, the dimensionless expression of ΔH is

$$\lambda = \frac{\Delta H}{H} = \frac{|\cos\alpha - \cos\beta|}{2(\cos\alpha + \cos\beta)}, \tag{18}$$

where λ is the dimensionless distance of the jet deviation from the central line and is determined by α and β only.

In existing studies on jets in circular tubes, the following method is used to analyze the influence of the contact angles on the jet velocity:[6,26]

$$\eta = \frac{v_j}{v_0} - 1, \tag{19}$$

where η is the flow-focusing efficiency, v_j is the maximum velocity of the jet, and v_0 is the average velocity of the incoming flow. For the jet

between the two plates in this study, if a similar v_0 exists, the flow-focusing effect can be readily calculated.

III. RESULTS AND DISCUSSION

A. Formation mechanism of the annular jet between two plates

The laser was focused on the bottom center of the droplet, generating high-temperature and high-pressure gas and plasma inside the droplet, accompanied by luminescence,[50,51] as shown in Fig. 4 (the bright area inside the droplet at 10 μs). Immediately, a hemispherical vapor bubble was created inside the droplet.[52,53] Owing to the constraints of the two plates, their shape developed rapidly from hemispherical to columnar in approximately 50 μs, as indicated by the blue arrow in Fig. 4(b). Simultaneously, the entire droplet expanded radially along the gap between the plates, driven by the internal vapor bubble. The experimental study focused on whether the droplet surface generated an annular jet during the expansion [shown by the red arrows in Figs. 4(b) and 4(c)] and the maximum velocity of the jet also generated.

In Fig. 4(a), the two hydrophobic plates allow the contact angles between the liquid surface and plates to reach nearly 90°, and the droplet surface is cylindrical. During the experiment, the edge shape is always straight (as indicated by the yellow arrow), which implies that the droplet surface maintains its cylindrical shape during the expansion. Therefore, when the upper and lower contact angles are both 90°, no jet is generated on the droplet surface; that is, only the circumferential curvature of the droplet cannot form a flow focus. In Fig. 4(b), the contact angles between the liquid surface and upper and lower plates are 62.9° and 60.9°, respectively, and the surface profile of the droplet is approximately a concave arc. During the expansion process, the inner concave extreme point of the liquid surface moves first, and the speed is significantly higher than that of the liquid on the upper and lower sides. After 100 μs, a distinct annular jet is observed. Under this condition, the jet thickness is large, and the maximum jet velocity is 5.25 m/s. In Fig. 4(c), the plate surfaces are superhydrophilic with contact angles of 18.0° and 11.0°. At 50 μs, the appearance of the jet can be distinguished, which then progresses to a finer annular jet. The maximum jet velocity reaches 10.27 m/s. Experiments show that the lateral shape of the droplet not only determines whether a jet is produced but also affects the shape of the jet. The quantitative relationship between the jet velocity and contact angles deserves further investigation, and the jet velocity also depends on the laser energy.[26]

However, it is difficult to accurately calculate the laser energy absorbed by the droplets in the experiments because of the losses in the energy transfer and conversion processes. In addition, because of the curvature of the droplet surface, the image is severely distorted when observing the vapor bubbles inside the droplet; therefore, further analysis is performed in combination with numerical simulations.

First, the jet profile shapes and velocity temporal curve of the jet tip obtained by the numerical simulations are compared with the experimental results. An experiment with contact angles of 18.0° and 11.0° was conducted to establish a numerical model, and the initial pressure (p_0) of the bubble inside the droplet was adjusted to obtain different jet velocities. When p_0 was 16.5 MPa, the numerical simulations were in perfect agreement with the experimental results. Figure 5(a) shows the evolution of the annular jet morphology in the first 200 μs, including the experiments and simulations. For the convenience of comparison, we intercepted the numerical simulation results on the vertical section along the radial direction. The jet morphology in the numerical simulation consistently agreed with the experimental results. Further analysis of the jet velocity, as shown in Fig. 5(b), indicates excellent agreement between the experimental and simulated velocity–time curves. In particular, they overlap around the maximum jet velocity, which is the most critical region for the analysis. Numerical simulations allow for a detailed analysis of the entire flow

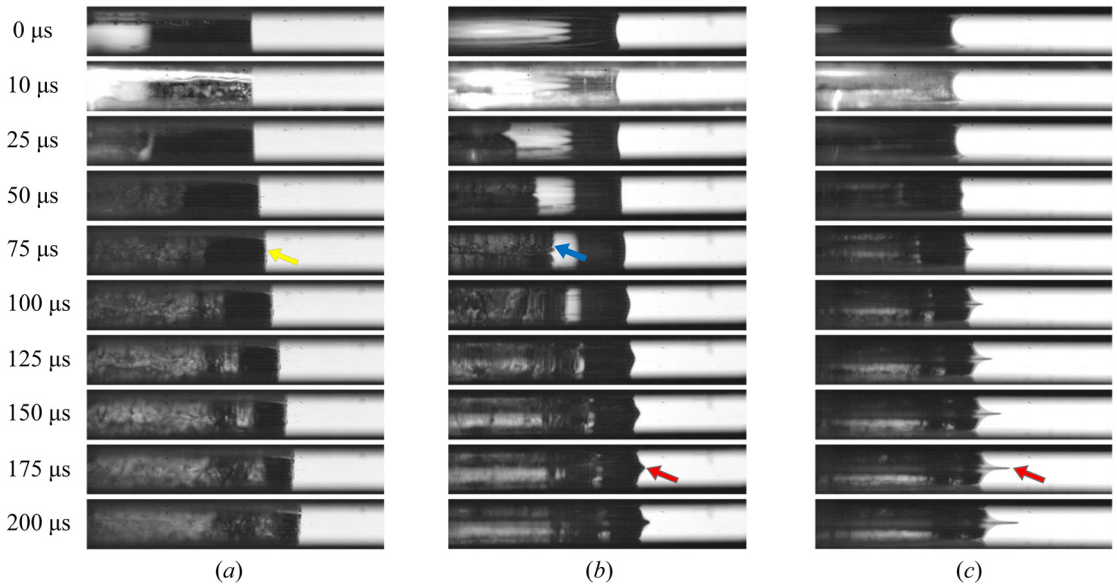

FIG. 4. Droplet surface annular jet experiments between parallel plates: (a) hydrophobic plates, (b) hydrophilic plates (no coating), and (c) superhydrophilic plates. Yellow arrow points the droplet surface without flow focus; blue arrow points the cavitation bubble inside the droplet; red arrows mark the annular jets.

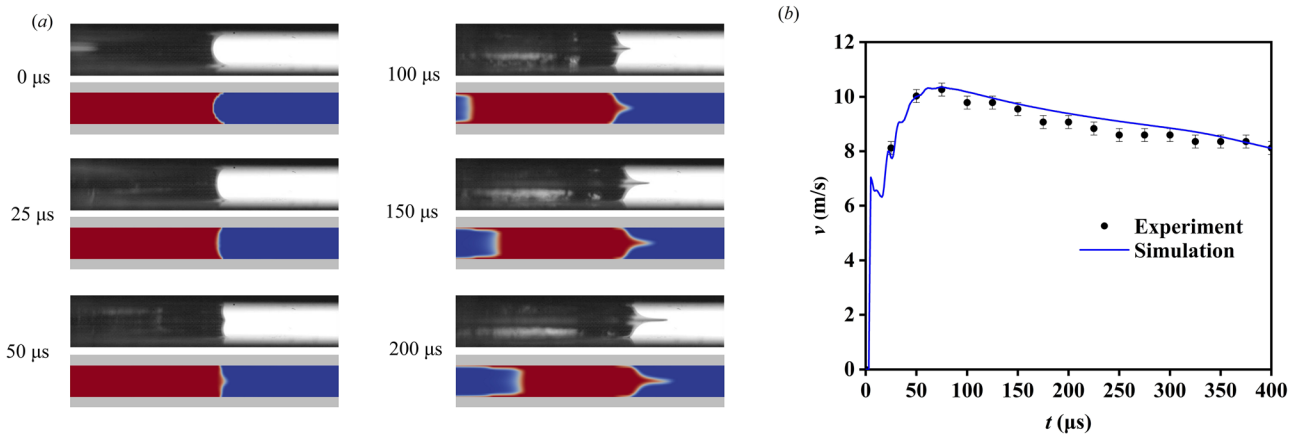

FIG. 5. Comparison of the simulation results of the annular jet with those of experiments ($\alpha = 11.0°$ and $\beta = 18.0°$). In the numerical simulation, the initial pressure of the bubble inside the droplet is 16.5 MPa. (a) Comparison of jet shape evolution. (The upper picture of each group is the experimental result, and the lower is the numerical simulation.) (b) Comparison of time–history curves of the horizontal velocity at the jet tip.

process, which provides insight into the mechanism of jet generation. Additionally, numerical simulations can flexibly set the contact angles to study the influence of the contact angles on the annular jet when the driving energy is consistent.

The flow profiles near the droplet surface are acquired from the numerical simulations, as shown in Fig. 6, which provides a means of investigating the mechanism of flow focusing to form an annular jet. As shown in Fig. 6(a), at 5 μs, the surface deformation of the droplet is negligible, and under the action of the pressure pulse, the velocity distribution on the droplet surface appears to be concentrated toward the center, which indicates that the surface shape is the key to determining the flow focusing. The initial interface shape determines this focusing tendency and persists for approximately 100 μs. Figures 6(b) and 6(c) show that the middle of the surface becomes flat or convex, and the fluid near the surface tends to concentrate toward the center. Compared to the velocity profile of the jet tip in Fig. 5(b), it is clear that the jet velocity continues to increase, reaching a maximum value of approximately 100 μs. As shown in Fig. 6(d), the velocity of the jet tip is greater than that of the root, and the jet becomes increasingly thinner with time. The flow-focusing mechanism of the annular jet between the two plates is similar to the formation principle of the jet in the circular tube, and the evolution of its velocity profiles is also similar.[54] The difference is that the concave liquid surface inside the circular tube is spherical, whereas the resulting jet is cylindrical. In this study, the droplet side was saddle-shaped, and the resulting jet was annular sheet-like. Compared to the jet in the circular tube with a diameter equal to the gap between the plates, the flux of the annular jet was significantly higher than that of the cylindrical jet at the same jet velocity.

B. Effect of the contact angles on the position of annular jets

When the upper and lower contact angles are approximately equal, as shown in Figs. 7(a) and 7(b), jets are generated near the middle of the two plates. However, as the difference between the contact angles is increased, the jet-generation positions move to the side of the plate with larger contact angles, as shown in Figs. 7(c) and 7(d). As shown in Eqs. (11) and (17), the sum of the cosines of the contact angles determines the curvature radius of the interface between the two plates with a constant distance, and the difference in cosines affects the location of generation of the jet.

Through the analysis of the experimental and numerical simulation results, the corresponding dimensionless jet offset distances λ_E and λ_S can be obtained and compared with λ calculated from Eq. (18), as shown in Figs. 8 and 9. The detailed calculation results are shown in Tables I and II. λ coincides perfectly with λ_E and λ_S, indicating that, ignoring gravity, the dimensionless offset distance of the jet depends only on the contact angles of the liquid surface with the two plates. As shown in Fig. 8, at the origin, $\alpha = \beta$, which means the jet position is on the centerline of the gap. When $\alpha > \beta$, the jet position is close to the lower plate, as shown in the red area. When $\alpha < \beta$, the jet position is close to the upper plate, as shown in the blue area. The lower border of the two regions indicates that for a certain value of $\cos\alpha - \cos\beta$, there exists a minimum value of λ ($\lambda_{\min}$). $\lambda_{\min}$ increases with the increase in the absolute value of the transverse axis, and the function is

$$\lambda_{\min} = \frac{|\cos\alpha - \cos\beta|}{2(\cos\alpha + \cos\beta)_{\max}}. \tag{20}$$

For $\alpha > \beta$,

$$\lambda_{\min} = \frac{\cos\beta - \cos\alpha}{4 - 2(\cos\beta - \cos\alpha)}, \tag{21}$$

and for $\alpha < \beta$,

$$\lambda_{\min} = \frac{\cos\alpha - \cos\beta}{4 - 2(\cos\alpha - \cos\beta)}. \tag{22}$$

C. Effect of contact angles on the focusing efficiency of annular jets

To study the velocity distribution inside the droplet during droplet expansion, a model with both upper and lower contact angles of 90° was established, and p_0 was set as 16.5 MPa. Annular jets were not

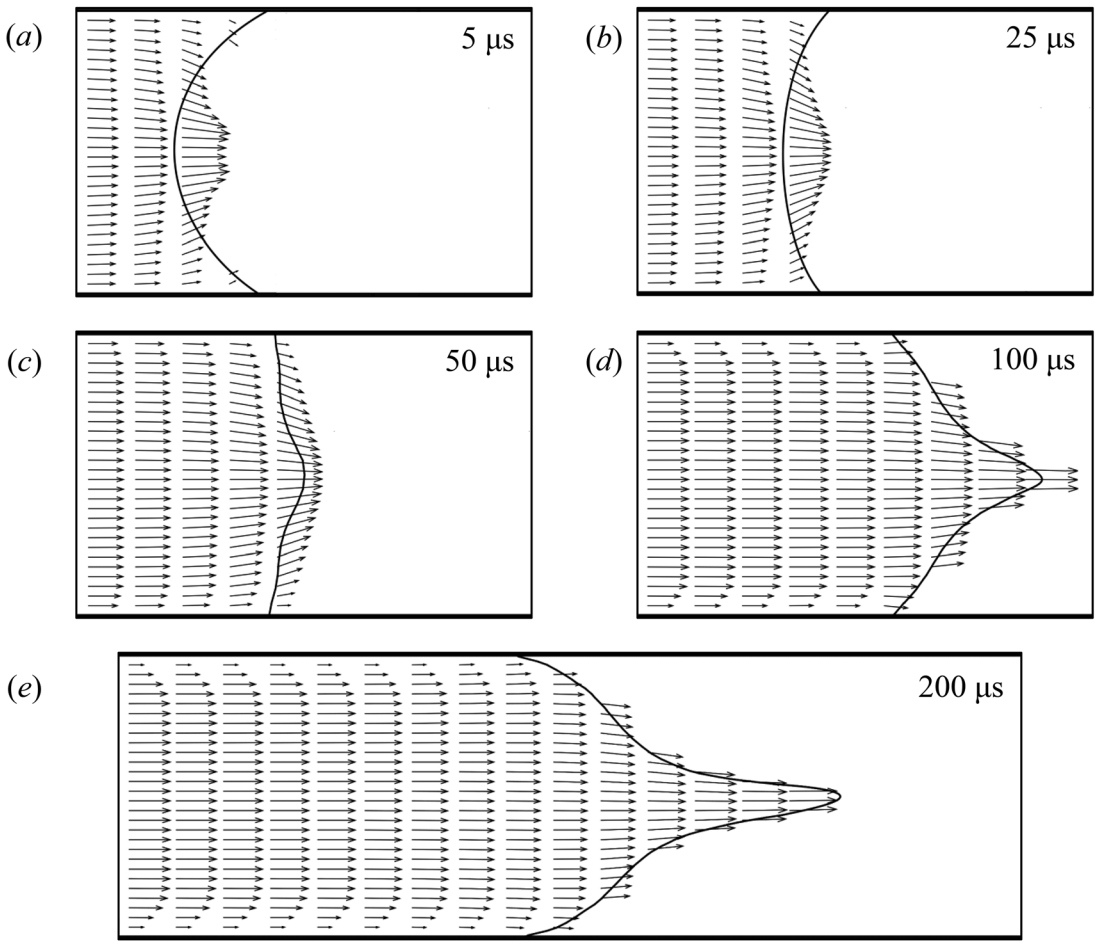

FIG. 6. Velocity fields during jet formation. The fields along the radius of the droplet and perpendicular to the plate, and their starting positions are the same in (a)–(e).

generated in this model. Figure 10 shows the distribution curves of the horizontal velocity (v) on the central axis of the droplet at four moments of time $t = 25$, 75, 125, and 175 μs. These four curves exhibit a common monotonically decreasing trend. This indicates that the velocity at each point on the horizontal central axis within the droplet varies during the droplet expansion and has no constant value.

Compared with the jet from the circular tube, the jet between the plates does not have a suitable incoming flow to calculate the focusing efficiency. Therefore, an alternative approach is considered, which is to obtain the maximum velocity that the outer surface of the droplet can achieve without flow focusing. On this basis, the increase in velocity owing to flow-focusing effects can be calculated. The inset in Fig. 10 shows the inner- and outer-surface velocity curves of the droplet. The inner-surface velocity (v_b) of the droplet rapidly increases to a maximum value in the first 25 μs and then decreases rapidly. However, after an initial rapid increase in the droplet outer-surface velocity (v_s), the growth rate slows down. At $t = 109$ μs, v_s achieves a maximum value ($v_{s\text{-max}}$) of 6.74 m/s. Considering $v_{s\text{-max}}$ as v_0 and substituting it into Eq. (19), η can be calculated together with v_j obtained by the experiments or simulations under the same conditions.

After obtaining an appropriate calculation method for the focusing efficiency, it is necessary to investigate the effect of the contact angles on the flow-focusing efficiency. First, the simple cases, in which the upper and lower contact angles are equal, are considered. The jet is positioned on the central line ($\lambda = 0$). As shown in Figs. 4(b) and 4(c), the basic understanding is that smaller the contact angle, smaller the curvature of the interface and greater the jet velocity. With the assistance of numerical methods, additional operating conditions can be set to investigate the effect of the contact angles on the focusing efficiency in detail. Keeping p_0 constant at 16.5 MPa, the upper and lower contact angles are set equally as 85°, 80°, 75°, 70°, 65°, 60°, 55°, 50°, 40°, 30°, 15°, and 0° in sequence. After obtaining v_j and v_0 through numerical simulation, the corresponding η is calculated using Eq. (19), as shown in Fig. 11, and the functional relationship can be fitted as

$$\eta = 0.548\left(\frac{\cos\alpha + \cos\beta}{2}\right)^{1.4}, \tag{23}$$

where $\alpha = \beta$. It should be noted that $\cos\alpha$ and $\cos\beta$ are not combined for consistency with the subsequent analysis. This indicates that the jet position is equidistant from the two plates, and the focusing efficiency

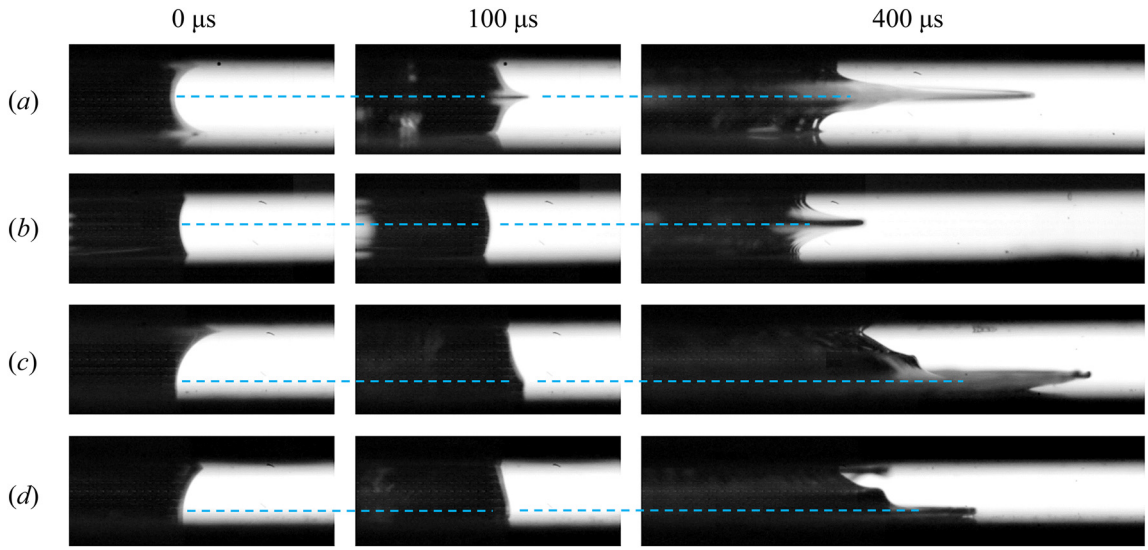

FIG. 7. Experimental images of the jet position at different contact angles. The blue dashed lines mark the jet-generation positions, and the detailed data of (a)–(d) are shown in Table I.

is proportional to the 1.4th power of the cosine of the contact angle. This result is consistent with the experimental results; when H is constant, a smaller R corresponds to a greater η. Because R cannot be infinitely small, the minimum R is $H/2$, that is, the contact angles are all zero and η reaches a maximum value of 0.548. This implies that the maximum velocity of the droplet surface can be increased by 54.8% under the action of focusing. Similar to the jet in the circular tube, η of the annular jet is positively related to the cosine of the contact angle.[26]

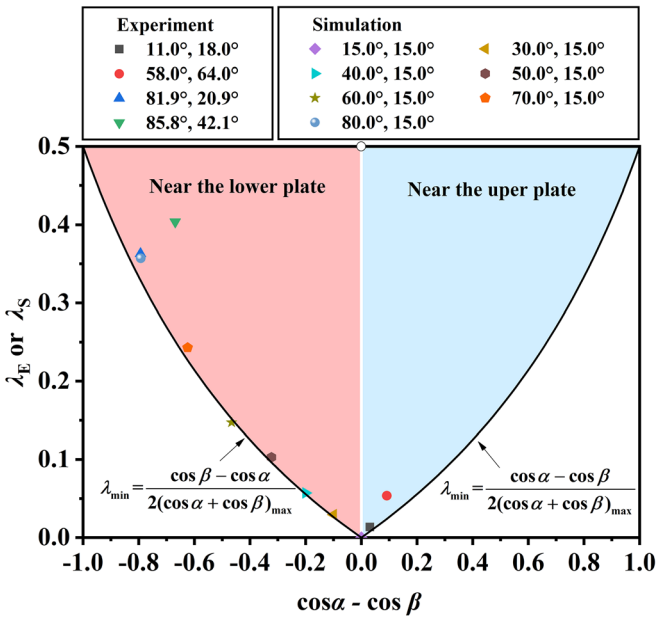

FIG. 8. Jet dimensionless offset distance at different contact angles.

For a better analysis of η when $\alpha \neq \beta$, seven groups of R are selected for numerical analysis. When H is constant, R can be represented as $\cos\alpha + \cos\beta$. Therefore, to ensure that each group of $\cos\alpha + \cos\beta$ is constant, the values of α and β are changed and the differences in α and β are measured by λ. Figure 12 shows the numerical results, where η exhibits two different tendencies as λ is increased. For cases where R is small, η increases with increasing λ, as in the cases of $\cos\alpha + \cos\beta > 0.5$. Conversely, when R is large, η decreases as λ increases. This implies that, in addition to R and λ, other factors also affect η.

As shown in Fig. 3, as α and β vary, the slope of the line connecting the points of contact between the droplet and plates (line AB)

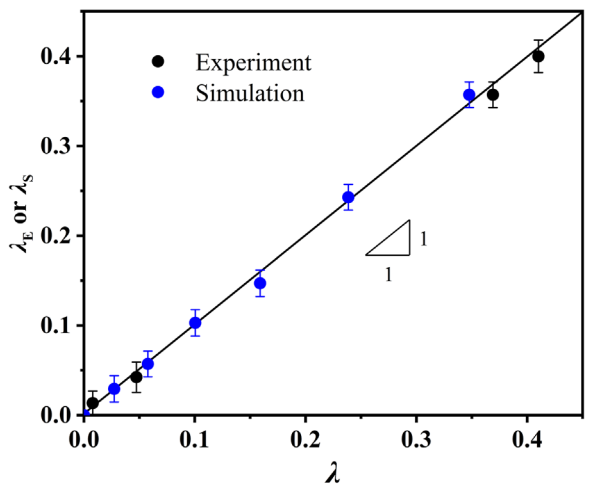

FIG. 9. Comparison of the experimental, simulated, and theoretical values of the jet dimensionless offset distance.

TABLE I. Comparison of the theoretical values of the jet position with experimental results.[a]

Number	A	β	λ	λ_E	Error (%)
a	11.0°	18.0°	0.007 9	0.013 5	−41.4
b	58.0°	64.0°	0.047 3	0.053 6	11.5
c	81.9°	20.9°	0.368 9	0.362 9	3.3
d	85.8°	42.1°	0.410 2	0.403 9	2.5

[a]The error caused by the image resolution is large when λ is close to zero.

TABLE II. Comparison of the theoretical values of the jet position with numerical simulation results.

Number	α	β	λ	λ_S	Error (%)
1	15.0°	15.0°	0	0	⋯
2	30.0°	15.0°	0.027 3	0.029 4	−7.3
3	40.0°	15.0°	0.057 7	0.057 1	1.0
4	50.0°	15.0°	0.100 4	0.102 9	−2.4
5	60.0°	15.0°	0.158 9	0.147 1	8.1
6	70.0°	15.0°	0.238 5	0.242 9	−1.8
7	80.0°	15.0°	0.347 6	0.357 1	−2.7

changes when R is constant. If the angle between the line AB and z-axis is Ψ, a geometric relationship of Ψ with α and β can be obtained

$$\psi = \frac{|\alpha - \beta|}{2}. \tag{24}$$

After further calculations,

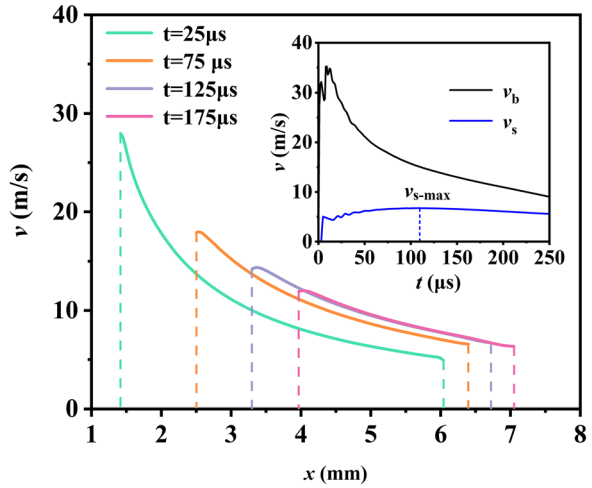

FIG. 10. The radial velocity distributions along the radial direction within the droplet at different moments; the horizontal axis is the distance from each point in the droplet to the initial center. The first and last ends of each curve indicate the inner-surface velocity (v_b) and outer-surface velocity (vs) of the droplet at that moment, respectively. The inset shows the change in the inner- and outer-surface velocities of the droplet with time and vs achieves a maximum value of 6.74 m/s at t = 109 μs.

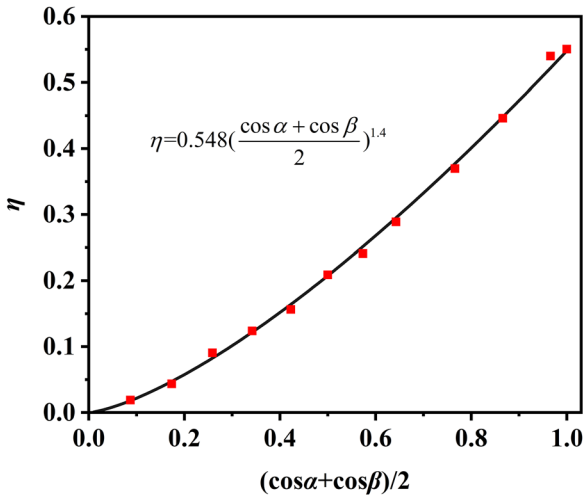

FIG. 11. Relationship between the focusing efficiency and contact angles ($\alpha = \beta$).

$$\tan\psi = \tan\frac{|\alpha - \beta|}{2} = \frac{L_{AB}}{H} = \frac{|\sin\alpha - \sin\beta|}{\cos\alpha + \cos\beta}, \tag{25}$$

where L_{AB} is the horizontal distance between the contact points of the droplet and the plates (points A and B). Therefore, $\tan\psi$ is determined only by α and β.

Considering R, λ, and $\tan\psi$ simultaneously and fitting all the data in Fig. 12, the results can adequately reflect the variation law of η with λ for different values of R (as shown by the solid lines in Fig. 12), and the equation is

$$\eta = 0.548\left(\frac{\cos\alpha + \cos\beta}{2}\right)^{1.4} + \lambda^3[9.142\tan\psi - 3.555\lambda], \tag{26}$$

where the first term represents the effect of R when $\lambda = 0$, the second term represents the effect of Ψ, and the third term represents the influence of λ. Clearly, η is determined only by α and β, and Eq. (23) is a

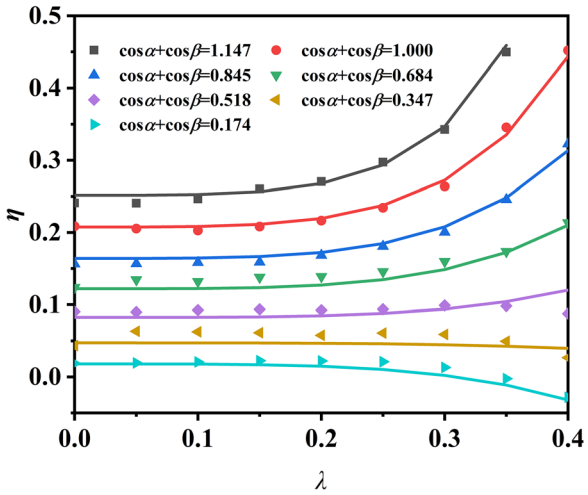

FIG. 12. Effect of the jet position offset on the jet focusing efficiency. The scattered data are obtained from numerical simulations, and the curves are given in Eq. (23).

special case, in which Eq. (26) takes the value of λ as 0. The coefficient of the second term is positive, indicating that a larger Ψ results in better focusing efficiency. However, λ also increases accordingly. As the jet is close to the plate surface, the corresponding flow resistance increases, which weakens the flow-focusing efficiency; thus, the third term coefficient is negative. When R is constant, competition exists between the second and third terms in Eq. (26) as the difference between α and β increases. The second term prevails when R is small and η increases with λ, which is consistent with the upper four curves in Fig. 12. Conversely, when R is larger, the third term has prominence and η decreases as λ increases, as shown by the bottom curve in Fig. 12. Near $\cos\alpha + \cos\beta = 0.5$, that is, $R = 2H$, η remains essentially constant as λ increases.

The variation in the contact angles affects the position of the jet and the inclination angle of the line connecting the upper and lower contact points. These two aspects jointly affect the flow-focusing efficiency.

IV. CONCLUSIONS

In this study, we investigate the effects of contact angles on dynamic characteristics of the annular focused jet by combinations of experiments, numerical simulations, and analytical modeling. The annular jet was generated from a droplet in a narrow gap between two plates when a laser-induced bubble expanded rapidly within it. The contact angles of the lower plate α and upper plate β ($\leq 90°$) were adjusted by changing the wettability of the plates. In the experiments, the gap height and the droplet radius were maintained. The experimental results show that the jet was generated at the centerline of the gap at $\alpha = \beta$. At $\alpha \neq \beta$, and the position of the jet got close to the plate with a larger contact angle.

Based on the flow characteristics of the droplet between the plates, a calculation method for the focusing efficiency of the annular jets is proposed. A theoretical model of the jet generation position and a semi-empirical relation for the focusing efficiency η are obtained. For the small fixed gap size (H), the jet generation position λ and the focusing efficiency η are only functions of the contact angles of α and β. We obtain (i) that η increases as the contact angle decreases at $\alpha = \beta$, and (ii) at $\alpha \neq \beta$, η increases and decreases with the increase in λ for $R < 2H$ and $R > 2H$, respectively.

Compared with a jet generated in a circular tube, the annular jet between the plates can regulate the position and intensity conveniently by adjusting the contact angle. Moreover, at the same size and velocity, the flux of the annular jet is significantly larger, which can improve the efficiency of related applications.

ACKNOWLEDGMENTS

This research was supported by the National Natural Science Foundation of China (Nos. 11872362 and 12122214), the Youth Innovation Promotion Association CAS (Nos. Y201906 and 2022019), and the National Key R&D Program of China (No. 2018FYA0305800).

AUTHOR DECLARATIONS

Conflict of Interest

The authors have no conflicts to disclose.

DATA AVAILABILITY

The data that support the findings of this study are available from the corresponding authors upon reasonable request.

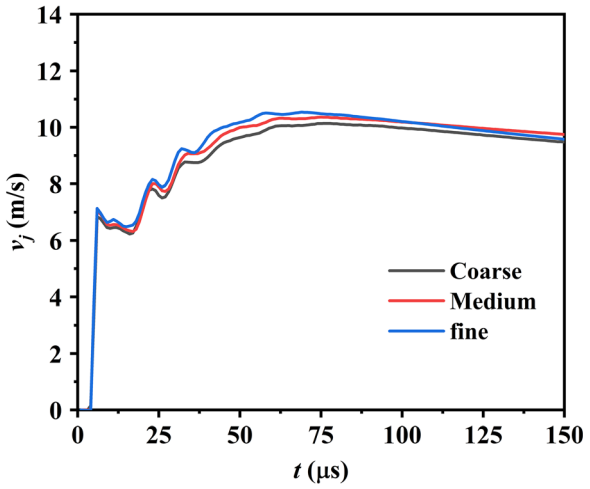

FIG. 13. Temporal evolution of the jet velocity using different grids.

APPENDIX: GRID INDEPENDENCE

We analyze the grid independence by three types of grids, namely, coarse, medium, and fine. Their numbers of cells are 644 800, 916 800, and 1 478 400, respectively. In our previously published research work, the grid independence of the temporal evolution of the bubble radius and outer edge of the droplet during the first pulsation of the cavitation bubble has been verified.[43] Here, we further verify the grid-independence of the maximum jet velocity. The initial conditions are the same as those in Fig. 5, namely, $\alpha = 11.0°$, $\beta = 18.0°$, and $P_0 = 16.5$ MPa. The jet time evolution calculated using different grids is shown in Fig. 13. The maximum velocity of the jet is 10.45 m/s calculated using the fine grid. The results are 10.27 and 10.05 m/s with medium and coarse grids, respectively. The differences are 1.8% and 3.8%. The errors are 1.8% and 3.8%. The results of the medium grid are consistent with those of the fine grid. Consequently, considering computational efficiency, we used the medium grid in all simulations.

REFERENCES

[1]J. Eggers and E. Villermaux, "Physics of liquid jets," Rep. Prog. Phys. **71**(3), 036601 (2008).
[2]S. K. Das, A. Dalal, M. Breuer, and G. Biswas, "Evolution of jets during drop impact on a deep liquid pool," Phys. Fluids **34**(2), 022110 (2022).
[3]W. Wang, F. Lin, X. Wei, and J. Zou, "Antibubble formation by a single drop impact on a free surface," Phys. Fluids **33**(4), 042107 (2021).
[4]A. Sarker, M. P. Boruah, P. R. Randive, and S. Pati, "The role of compound droplet size on transition from jetting to bubble entrapment during its impact on liquid," Phys. Fluids **33**(10), 102103 (2021).
[5]Z. Wang, R. Duan, L. Liu, and H. Yang, "Jetting behavior as a bubble bursts in free space," Phys. Fluids **33**(2), 023304 (2021).
[6]A. Antkowiak, N. Bremond, S. L. Dizes, and E. Villermaux, "Short-term dynamics of a density interface following an impact," J. Fluid Mech. **577**, 241–250 (2007).
[7]T. Séon and A. Antkowiak, "Large bubble rupture sparks fast liquid jet," Phys. Rev. Lett. **109**(1), 014501 (2012).
[8]D. K. Raja and S. P. Das, "Effect of liquid depth on dynamics and collapse of large cavities generated by standing waves," Phys. Fluids **33**(1), 012110 (2021).

[9]Y. Zhang, T. Guo, P. Vlachos, and A. M. Ardekani, "Velocity scaling and breakup criteria for jets formed due to acceleration and deceleration process," Phys. Rev. Fluids **5**(7), 074003 (2020).
[10]E. Mahravan and D. Kim, "Bubble collapse and jet formation inside a liquid film," Phys. Fluids **33**(11), 112102 (2021).
[11]B. Mohajer, A. Dey, and R. Li, "Stagnation line due to colliding wall jets of two liquid impinging jets on a horizontal surface," Phys. Fluids **33**(4), 047112 (2021).
[12]J. Krizek, B. Lavickova, and C. Moser, "Degradation study on molecules released from laser-based jet injector," Int. J. Pharm. **602**, 120664 (2021).
[13]A. Mohizin and J. K. Kim, "Current engineering and clinical aspects of needle-free injectors: A review," J. Mech. Sci. Technol. **32**(12), 5737–5747 (2018).
[14]H. Tan, "An adaptive mesh refinement based flow simulation for free-surfaces in thermal inkjet technology," Int. J. Multiphase Flow **82**, 1–16 (2016).
[15]P. Delrot, M. A. Modestino, F. Gallaire, D. Psaltis, and C. Moser, "Inkjet printing of viscous monodisperse microdroplets by laser-induced flow focusing," Phys. Rev. Appl. **6**(2), 024003 (2016).
[16]E. Antonopoulou, O. G. Harlen, M. Rump, T. Segers, and M. A. Walkley, "Effect of surfactants on jet break-up in drop-on-demand inkjet printing," Phys. Fluids **33**(7), 072112 (2021).
[17]K. B. Fritzler and V. Y. Prinz, "3D printing methods for micro-and nanostructures," Phys.-Usp. **62**(1), 54–69 (2019).
[18]H. E. Orimi, S. S. Hosseini Kolkooh, E. Hooker, S. Narayanswamy, B. Larrivée, and C. Boutopoulos, "Drop-on-demand cell bioprinting via laser induced side transfer (LIST)," Sci. Rep. **10**(1), 9730 (2020).
[19]S. Xiong, L. K. Chin, K. Ando, T. Tandiono, A. Q. Liu, and C. D. Ohl, "Droplet generation via a single bubble transformation in a nanofluidic channel," Lab Chip **15**(6), 1451–1457 (2015).
[20]S. R. Gonzalez Avila, C. Song, and C. D. Ohl, "Fast transient microjets induced by hemispherical cavitation bubbles," J. Fluid Mech. **767**, 31–51 (2015).
[21]E. Turkoz, S. Kang, L. Deike, and C. B. Arnold, "Subthreshold laser jetting via flow-focusing in laser-induced forward transfer," Phys. Rev. Fluids **3**(8), 082201 (2018).
[22]J. Krizek, P. Delrot, and C. Moser, "Repetitive regime of highly focused liquid microjets for needle-free injection," Sci. Rep. **10**(1), 5067 (2020).
[23]Y. Tagawa, N. Oudalov, A. E. Ghalbzouri, C. Sun, and D. Lohse, "Needle-free injection into skin and soft matter with highly focused microjets," Lab Chip **13**(7), 1357–1363 (2013).
[24]Y. Miyazaki, M. Usawa, S. Kawai, J. Z. Yee, M. Muto, and Y. Tagawa, "Dynamic mechanical interaction between injection liquid and human tissue simulant induced by needle-free injection of a highly focused microjet," Sci. Rep. **11**(1), 14544 (2021).
[25]E. Turkoz, S. Kang, X. Du, L. Deike, and C. B. Arnold, "Reduction of transfer threshold energy for laser-induced jetting of liquids using faraday waves," Phys. Rev. Appl. **11**(5), 054022 (2019).
[26]Y. Tagawa, N. Oudalov, C. W. Visser, I. R. Peters, D. van der Meer, C. Sun, and D. Lohse, "Highly focused supersonic microjets," Phys. Rev. X **2**(3), 031002 (2012).
[27]R. Bergmann, E. De Jong, J. B. Choimet, D. Van Der Meer, and D. Lohse, "The origin of the tubular jet," J. Fluid Mech. **600**, 19–43 (2008).
[28]T. W. Killian, R. A. Klaus, and T. T. Truscott, "Rebound and jet formation of a fluid-filled sphere," Phys. Fluids **24**(12), 122106 (2012).
[29]W. Zhao, S. Lin, L. Chen, E. Q. Li, S. T. Thoroddsen, and M. J. Thoraval, "Jetting from an impacting drop containing a particle," Phys. Fluids **32**(1), 011704 (2020).
[30]E. Ghabache, T. Seon, and A. Antkowiak, "Liquid jet eruption from hollow relaxation," J. Fluid Mech. **761**, 206–219 (2014).
[31]G. Zhang, Y. Zhu, J. Yang, and M. Sun, "Liquid jets produced by an immersed electrical explosion in round tubes," Phys. Fluids **29**(6), 062102 (2017).
[32]M. Jalaal, M. Klein Schaarsberg, C. W. Visser, and D. Lohse, "Laser-induced forward transfer of viscoplastic fluids," J. Fluid Mech. **880**, 497–513 (2019).
[33]Y. Saade, M. Jalaal, A. Prosperetti, and D. Lohse, "Crown formation from a cavitating bubble close to a free surface," J. Fluid Mech. **926**, A5 (2021).
[34]Z. Wang, Y. Tian, C. Zhang, Y. Wang, and W. Deng, "Massively multiplexed electrohydrodynamic tip streaming from a thin disc," Phys. Rev. Lett. **126**(6), 064502 (2021).
[35]A. Lafuma and D. Quere, "Superhydrophobic states," Nat. Mater. **2**(7), 457–460 (2003).
[36]M. Fortes, "Axisymmetric liquid bridges between parallel plates," J. Colloid Interface Sci. **88**(2), 338–352 (1982).
[37]V. Suponitsky, D. Plant, E. J. Avital, and A. Munjiza, "Pressure wave in liquid generated by pneumatic pistons and its interaction with a free surface," Int. J. Appl. Mech. **9**(3), 1750037 (2017).
[38]Q. Zeng, S. R. Gonzalez-Avila, S. T. Voorde, and C.-D. Ohl, "Jetting of viscous droplets from cavitation-induced Rayleigh–Taylor instability," J. Fluid Mech. **846**, 916–943 (2018).
[39]B. Han, K. Kohler, K. Jungnickel, R. Mettin, W. Lauterborn, and A. Vogel, "Dynamics of laser-induced bubble pairs," J. Fluid Mech. **771**, 706–742 (2015).
[40]R. I. Issa, "Solution of the implicitly discretised fluid flow equations by operator-splitting," J. Comput. Phys. **62**(1), 40–65 (1986).
[41]M. Koch, C. Lechner, F. Reuter, K. Kohler, R. Mettin, and W. Lauterborn, "Numerical modeling of laser generated cavitation bubbles with the finite volume and volume of fluid method, using OpenFOAM," Comput. Fluids **126**, 71–90 (2016).
[42]B. Ye, Y. Wang, C. Huang, and J. Huang, "Numerical study of the pressure wave-induced shedding mechanism in the cavitating flow around an axisymmetric projectile via a compressible multiphase solver," Ocean Eng. **187**, 106179 (2019).
[43]J. Wang, H. Li, W. Guo, Z. Wang, T. Du, Y. Wang, A. Abe, and C. Huang, "Rayleigh-Taylor instability of cylindrical water droplet induced by laser-produced cavitation bubble," J. Fluid Mech. **919**, A42 (2021).
[44]Q. Y. Zeng, H. J. An, and C. D. Ohl, "Wall shear stress from jetting cavitation bubbles: Influence of the stand-off distance and liquid viscosity," J. Fluid Mech. **932**, A14 (2022).
[45]Q. Y. Zeng, S. R. Gonzalez-Avila, R. Dijkink, P. Koukouvinis, M. Gavaises, and C. D. Ohl, "Wall shear stress from jetting cavitation bubbles," J. Fluid Mech. **846**, 341–355 (2018).
[46]M. A. C. Teixeira, S. Arscott, S. J. Cox, and P. I. C. Teixeira, "When is a surface foam-phobic or foam-philic?," Soft Matter **14**(26), 5369–5382 (2018).
[47]H. N. G. Nguyen, O. Millet, C. F. Zhao, and G. Gagneux, "Theoretical and experimental study of capillary bridges between two parallel planes," Eur. J. Environ. Civ. Eng. **26**, 1198 (2020).
[48]P. I. C. Teixeira and M. A. C. Teixeira, "The shape of two-dimensional liquid bridges," J. Phys.: Condens. Matter **32**(3), 034002 (2020).
[49]D. K. Raja, S. P. Das, and E. J. Hopfinger, "Extreme singular events associated with inertial-viscous cusp formation in fluids," Phys. Fluids **32**, 062104 (2020).
[50]S. T. Thoroddsen, K. Takehara, T. G. Etoh, and C. D. Ohl, "Spray and microjets produced by focusing a laser pulse into a hemispherical drop," Phys. Fluids **21**(11), 112101 (2009).
[51]P. Koukouvinis, M. Gavaises, O. Supponen, and M. Farhat, "Simulation of bubble expansion and collapse in the vicinity of a free surface," Phys. Fluids **28**(5), 052103 (2016).
[52]Q. Y. Zeng, S. R. Gonzalez-Avila, and C. D. Ohl, "Splitting and jetting of cavitation bubbles in thin gaps," J. Fluid Mech. **896**, A28 (2020).
[53]S. R. Gonzalez-Avila, A. C. Van Blokland, Q. Y. Zeng, and C. D. Ohl, "Jetting and shear stress enhancement from cavitation bubbles collapsing in a narrow gap," J. Fluid Mech. **884**, A23 (2020).
[54]I. R. Peters, Y. Tagawa, N. Oudalov, C. Sun, A. Prosperetti, D. Lohse, and D. Van Der Meer, "Highly focused supersonic microjets: Numerical simulations," J. Fluid Mech. **719**, 587–605 (2013).